Acta Geotechnica (2021) 16:399–419
https://doi.org/10.1007/s11440-020-01012-9

RESEARCH PAPER

Investigating the effect of flow direction on suffusion and its impacts on gap-graded granular soils

Hao Xiong[1] · Zhen-Yu Yin[2] · Jidong Zhao[3] · Yi Yang[4]

Received: 13 February 2020 / Accepted: 17 June 2020 / Published online: 7 July 2020

Abstract
The flow direction is generally different from the gravity direction in geotechnical structures or slopes, the effect of which during suffusion remains unclear. This paper presents a coupled computational fluid dynamics and discrete element method approach to simulate the particle–fluid interaction relevant to this problem. The CFD-DEM approach is first benchmarked by a classic granular system problem, which is then used to investigate the characteristics of suffusion and its impact on the mechanical behavior. Five different angles between gravity and seepage directions for gap-graded soils with two fines contents are examined. Both the macroscopic and microscopic characteristics during suffusion and triaxial loading tests are analyzed. The direction angle is found to play a significant role affecting the erosion process and the mechanical consequence of soils. The results show that the greater the angle is, the harder it is for suffusion to occur and continue.

Keywords Computational fluid dynamics · Discrete element method · Granular soil · Internal erosion · Microstructure · Solid–fluid interaction

1 Introduction

Internal erosion of fine particles in gap-graded granular soils induced by fluid flow is one of the most common causes of failure in hydraulic earth structures (e.g., levees, embankment dams) and slopes where the flow direction is generally different from the gravity direction in different locations, as shown in Fig. 1. As noted by [14], approximately 0.5% of the embankment dams worldwide exhibit failure due to internal erosion. Moreover, statistical analysis has shown that internal erosion is the governing failure mode of approximately half of all failures of embankment dams [40]. Typically, internal erosion presents itself in many different forms, which can be classified into four types [14]: (1) concentrated leak: seeping water erodes and enlarges a crack until a breach occurs; (2) backward erosion: initiated at the exit point of the seepage path, a pipe forms backward from the exit point until breach; (3) contact erosion: the particles from the finer layer are eroded into the coarser layer; and (4) suffusion: finer soil particles are eroded through the voids between coarser particles. This study focuses on suffusion involving the selective erosion of fine particles within the matrix of coarse particles.

Most previous studies have focused on theoretically macroscopic behaviors of the soil mass and experimental descriptions of the internal erosion mechanism [2, 34, 45, 47, 50, 51, 54]. It should be acknowledged that theoretical research and physical experiments have made much progress in this research field [1, 31, 32, 67]. However, internal erosion is a multidisciplinary process that is governed by the principles of soil mechanics and hydraulics. Owing to the complexity of internal erosion hiding

✉ Zhen-Yu Yin
zhenyu.yin@polyu.edu.hk; zhenyu.yin@gmail.com

Hao Xiong
haoxiong19529@szu.edu.com

[1] College of Civil and Transportation Engineering, Shenzhen University, Shenzhen, People's Republic of China

[2] Department of Civil and Environmental Engineering, The Hong Kong Polytechnic University, Hung Hom, Kowloon, Hong Kong, People's Republic of China

[3] Department of Civil and Environmental Engineering, Hong Kong University of Science and Technology, Clear Water Bay, Kowloon, Hong Kong, People's Republic of China

[4] Department of Civil Engineering, Chu Hai College of Higher Education, Hong Kong, People's Republic of China

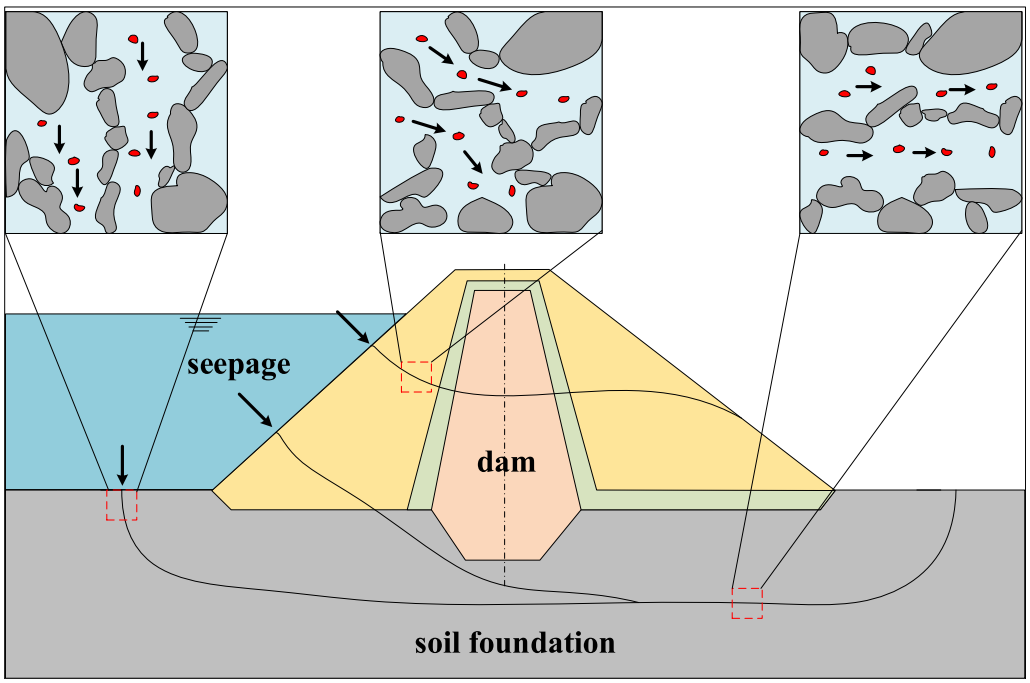

Fig. 1 Schematic of different seepage directions in a dam

behind the macroscopic level, these studies have limitations in their understanding of such a complicated issue from the macroscopic viewpoint. To gain a better understanding, particularly from a microscopic level, some numerical techniques have been proposed. For instance, [9] introduced a two-dimensional coupled discrete element method and lattice Boltzmann method (DEM-LBM) [8, 15] to study the soil erosion induced by local leakage from a buried pipe. This method was then applied to a three-dimensional problem by [55] to investigate soil erosion in granular filters. [56] used a coupled discrete element method and pore-scale finite volume method (DEM-PFV) [6, 46] to study the internal erosion problem on the representative elementary volume (REV) scale, investigating the underlying mechanical instability of granular materials by impacting fluid flow. A combination of computational fluid dynamics (CFD) and the discrete element method (DEM) has also been widely used to model the particle–fluid system in recent studies, such as [7, 17, 20, 23, 29, 49, 64, 66]. The CFD-DEM approach is selected in this study for three main reasons: (1) both open-source CFD (OpenFOAM) and DEM (LIGGGHTS) packages are available and have high-performance parallel computing efficiencies; (2) the approach provides more realistic simulations of fluid–particle interactions; and (3) the approach is capable of capturing both micro- and macro-characteristics of particle and fluid, providing new insights into the microstructural origins underpinning the macroscopic failure of internal erosion.

So far, previous studies have focused on the initiation and development of internal erosion, with few of them focusing on the resulting mechanical properties. In the literature, several experimental studies have been conducted to characterize the post-erosion properties of soils. For example, [4, 5] carried out drained triaxial compression tests on eroded soils and noticed that after the loss of a significant amount of fine particles, the original dilatant stress–strain behavior became contractant and the peak stress decreased. In addition, [24, 25] attributed the reduction in soil strength to the loss of fine particles actively engaged in the mechanical transfer and spatial rearrangement of soil particles, which may adjust the force transfer. [37] pointed out that internal erosion is obviously not homogeneous, highlighting the existence of preferential flow paths that lead to a heterogeneous sample in terms of the fine particles, void ratio and intergranular void ratio distribution. On the other hand, [48] presented the effect of fines content on the mechanical behavior in a bidisperse (or gap-graded) soil from a numerical point of view. Other numerical studies, such as [18, 19, 36, 41], investigated the mechanical consequences of erosion by particle removal at different loading states but fell short of performing fully coupled fluid flow. However, there is a lack of studies focusing on the effect of the angle between the flow direction and gravity during internal erosion and its impact on the mechanics of gap-graded granular soils.

The main objective of this paper is to study suffusion and its resulting mechanical properties in gap-graded soils

by using a coupled CFD-DEM approach with an emphasis on the effect of the angle between the flow direction and gravity. After benchmarking the particle–fluid interaction approach, a cuboidal soil sample is prepared to simulate suffusion in six different conditions, i.e., one case without considering gravity and five cases considering different angles between the flow direction and gravity. For each case, two fines content (FC) values of 15% and 35% are selected. The effect of the angle between the different directions of gravity and seepage is thus investigated. A comparison of the mechanical properties at states before and after suffusion is made from both microscopic and macroscopic points of view.

2 CFD-DEM coupling approach

The CFD-DEM coupling approach used in this study is based on two open-source packages. The CFD package is used within the framework of *OpenFOAM-5.x*, and the DEM package is executed by *LIGGGHTS-PUBLIC-3.8*. The DEM package is developed for modeling granular material based on *LAMMPS*, which is an open-source molecular dynamics code developed by Sandia National Laboratories (Los Alamos, New Mexico)[39].

2.1 Governing equations of the DEM

In the DEM [10], the motion of particles is governed by Newton's laws of motion, and the particles are tracked in a Lagrangian way. The forces that act on the particles in this simulation include the normal force and tangential force from the particle contacts, the drag force and buoyancy force from the fluid part, and gravity. For a particle i in the particle system, the kinematic function is expressed as

$$\begin{aligned} m_i \frac{dv_i}{dt} &= \sum_j F_{ij}^n + \sum_j F_{ij}^t + F_i^f + F_i^g \\ I_i \frac{d\omega_i}{dt} &= r_i \times \sum_j F^t + T_i, \end{aligned} \tag{1}$$

where v_i and ω_i denote the translational and angular velocities of particle i, respectively. F_{ij}^n and F_{ij}^t are the contact force and contact torque acting on particle i by particle j or the wall(s), respectively. F^f is the particle–fluid interaction force acting on particle i. F_i^g is the gravitational force, and m_i and I_i are the mass and moment of inertia of particle i, respectively. In *LIGGGHTS*, the Hertz-Mindlin contact model is employed in conjunction with Coulomb's friction law to describe the interparticle contact behavior.

2.2 Governing equations of the CFD

The literature provides a number of different ways to treat the fluid phase, some of which were collected by [70]. In the presented CFD-DEM coupling approach, both the fluid and the solid pressures are included in the fluid governing equation. This means that the continuous fluid domain is discretized into cells in the CFD method. The CFD will solve the following governing equations at each cell for the locally averaged state variables such as fluid velocity, pressure and density:

$$\begin{aligned} &\frac{\partial \rho_f \alpha_f}{\partial t} + \nabla \cdot (\rho_f \alpha_f \boldsymbol{u}_f) = 0 \\ &\frac{\partial (\alpha_f \rho_f \boldsymbol{u}_f)}{\partial t} + \nabla \cdot (\alpha_f \rho_f \boldsymbol{u}_f \boldsymbol{u}_f) - \nabla \cdot (\alpha_f \boldsymbol{\tau}_f) \\ &= -\alpha_f \nabla p + \boldsymbol{R}_{sl} + \alpha_f \rho_f \boldsymbol{g}, \end{aligned} \tag{2}$$

where α_f and α_s are the fluid and soil fractions, respectively, with $\alpha_f = 1 - \alpha_s$; the density of the fluid is given by ρ_f; $\boldsymbol{u}_f$ is the average velocity of a fluid cell; p is the fluid pressure in the cell; $\boldsymbol{\tau}_f$ is the stress tensor for the fluid phase; and $\boldsymbol{R}_{sl}$ is the momentum exchange with the particulate phase and is expressed as

$$\boldsymbol{R}_{sl} = \frac{|\sum F_i^f|}{V_{cell} \cdot |\boldsymbol{u}_f - \boldsymbol{u}_p|} (\boldsymbol{u}_f - \boldsymbol{u}_p). \tag{3}$$

2.3 Fluid–particle interaction forces

In this study, the predominant forces are the drag force $\boldsymbol{f}_d$ and the pressure gradient force $\boldsymbol{f}_{\nabla p}$. Other fluid–particle interaction forces are neglected. Thus, the total fluid–particle interaction force $\boldsymbol{f}_{p,f}$ is calculated as

$$\boldsymbol{f}_{p,f} = \boldsymbol{f}_d + \boldsymbol{f}_{\nabla p}. \tag{4}$$

The pressure gradient force is expressed as $\boldsymbol{f}_{\nabla p} = -V_p \nabla p$. One of the force models used for the presented calculations was developed by [27] and [28]. In the formulation used by [53], the force term for the drag is given by

$$\boldsymbol{f}_d = \frac{V_p \beta}{\alpha_s} (\boldsymbol{u}_f - \boldsymbol{u}_p), \tag{5}$$

where V_p is the volume of the considered particle and β denotes the interphase momentum exchange term. The pressure gradient force is expressed as $\boldsymbol{f}_{\nabla p} = -V_p \nabla p$.

2.4 CFDEM coupling method

CFDEM coupling is based on an open-source CFD-DEM engine that enables the parallel calculation of the DEM solver of *LIGGGHTS* and the CFD package *OpenFOAM*.

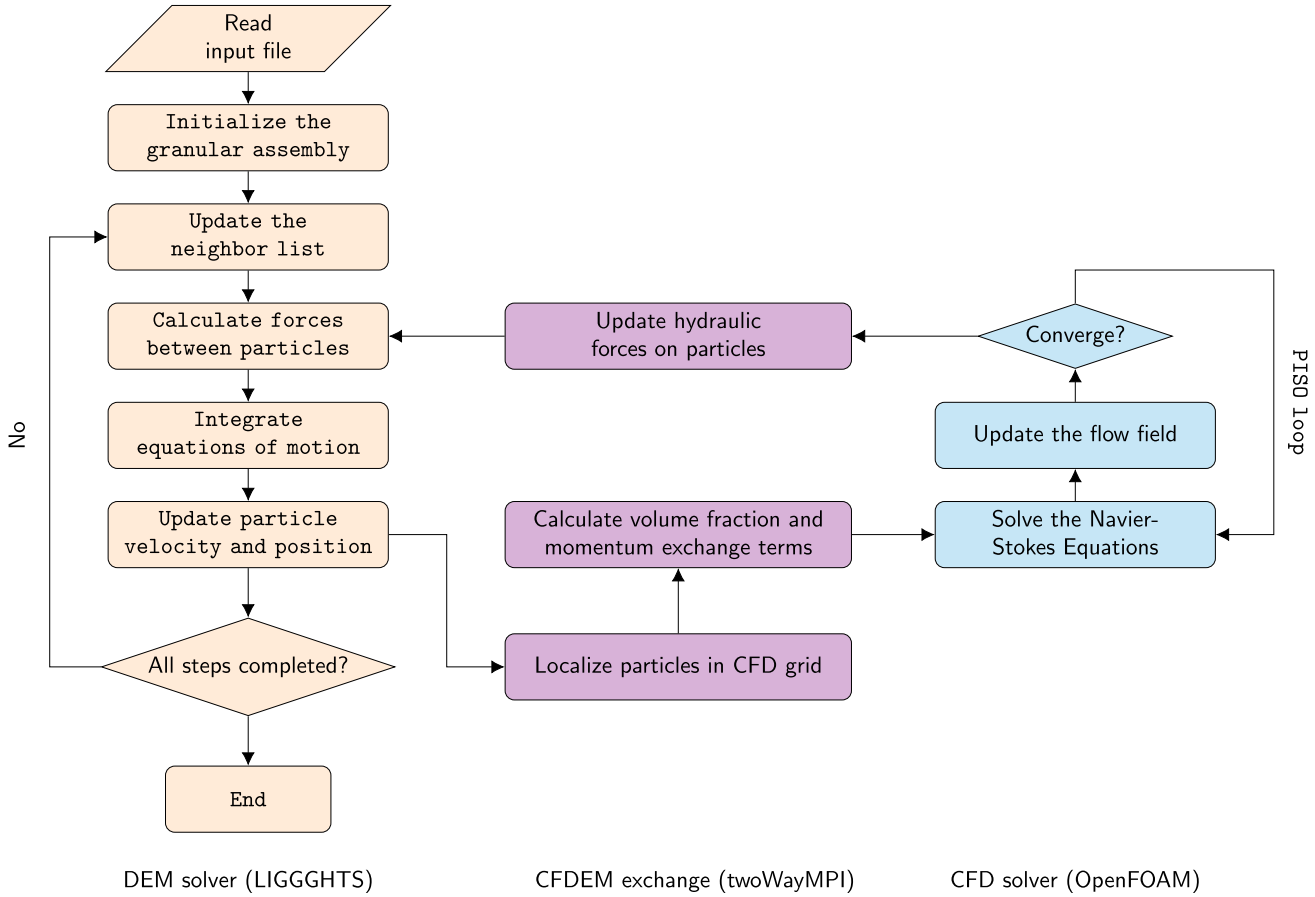

Fig. 2 Algorithm flowchart of CFDEM coupling

In this study, the coupling solver called 'cfdemSolverPiso' [16] is used, which is a finite volume-based solver for turbulent Navier–Stokes equations applying the pressure-implicit-split-operator (PISO) algorithm. The CFDEM algorithm flowchart is shown in Fig. 2 and can be illustrated by following steps:

1. The DEM first reads an input file to prepare a granular assembly. The neighbor list, including contact points and overlaps for each particle, is built. The Hertz constitutive model is then applied to each contact to calculate forces and momentum. By using Newton's second law, the motion of each particle is obtained. Last, the velocities and positions of all particles are updated accordingly.
2. The information for all particles is packed and transferred to the CFD via a twoWayMPI data exchange method. Before the data reach the CFD solver, the CFDEM engine determines which CFD grid the particle localizes. Both the volume fraction and the mean particle velocity in each CFD cell are then calculated.
3. For the CFD solver, the PISO algorithm (more information is given in [21, 22]) is used. Rather than solve all of the coupled equations in a coupled or iterative sequential fashion, PISO splits the operators into an implicit predictor and multiple explicit corrector steps. This scheme is not thought of as iterative, and very few corrector steps are necessary to obtain the desired accuracy.
4. When the PISO loop converges, the CFDEM engine updates the hydraulic forces on all particles and then returns the data to the DEM solver. These forces calculated by the CFD part participate in the calculation of the DEM as part of the force acting on the particles. The DEM solver cycles steps until the simulation finishes.

2.5 Benchmarks of the CFDEM coupling approach

The coupled CFDEM approach has been widely verified by many researchers, such as [7, 26, 29, 38, 42, 66]. In this study, the Ergun test [12] is examined. As shown in Fig. 3,

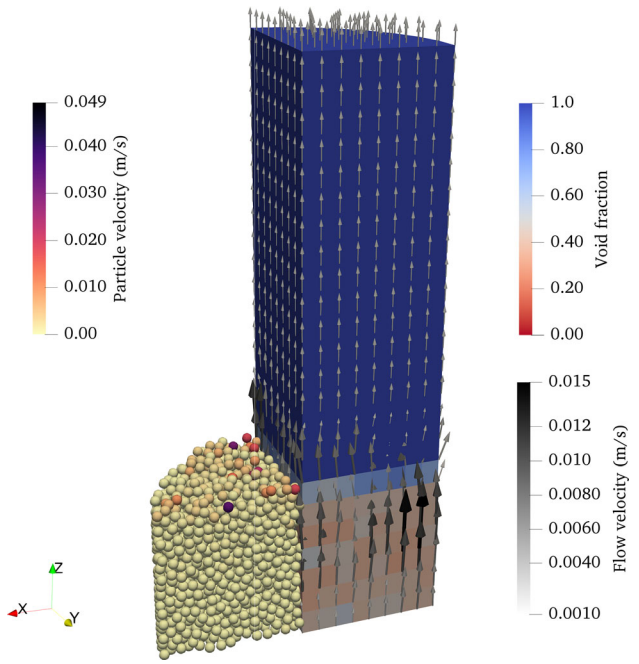

Fig. 3 Ergun test: particle bed fluidizes at predicted minimal fluidization velocity v_{mf}, rendering DEM part only on the left and CFD part only on the right

the Ergun test describes fluid flow through a granular column. It is worth noting that Fig. 3 only renders the DEM part on the left and the CFD part on the right. The fluid flows in from the bottom surface of the cylinder at a constant speed and flows out from the top surface. The surrounding surface of the cylinder is a non-permeable boundary. Due to gravity, particles are deposited at the bottom of the cylinder. As expressed by the Ergun equation, the pressure drop Δp is a quadratic function of the superficial velocity v_s, which is the velocity that the fluid would have through an empty tube at the same volumetric flow rate. This can be expressed as:

$$\Delta p = \frac{150\mu L(1-e)^2}{d^2 e^3} v_s + \frac{1.75L\rho(1-e)}{de^3} v_s|v_s|, \tag{6}$$

where Δp is the pressure drop across the bed, $L = 0.0156$m is the length of the bed, $d = 0.001$m is the equivalent spherical diameter of the packing, $\rho = 10\text{kg/m}^3$ is the density of the fluid, $\mu = 1.5 \times 10^{-3}$Pa is the dynamic viscosity of the fluid, $e = 0.45$ is the void fraction of the bed, and v_s is the superficial velocity.

Figure 4 shows good agreement between the experimental data and the numerical results. When a certain minimal fluidization velocity v_{mf} is reached, the granular packing will fluidize, resulting in a constant pressure drop despite the increasing fluid velocity.

3 Model setup and test program for suffusion

3.1 Model setup and parameter selection

In this study, a cuboid sample is modeled with a size of 13 mm×13 mm×20 mm ($14D_{50} \times 14D_{50} \times 21.5D_{50}$, as shown in Fig. 5). The cuboid sample is confined by six

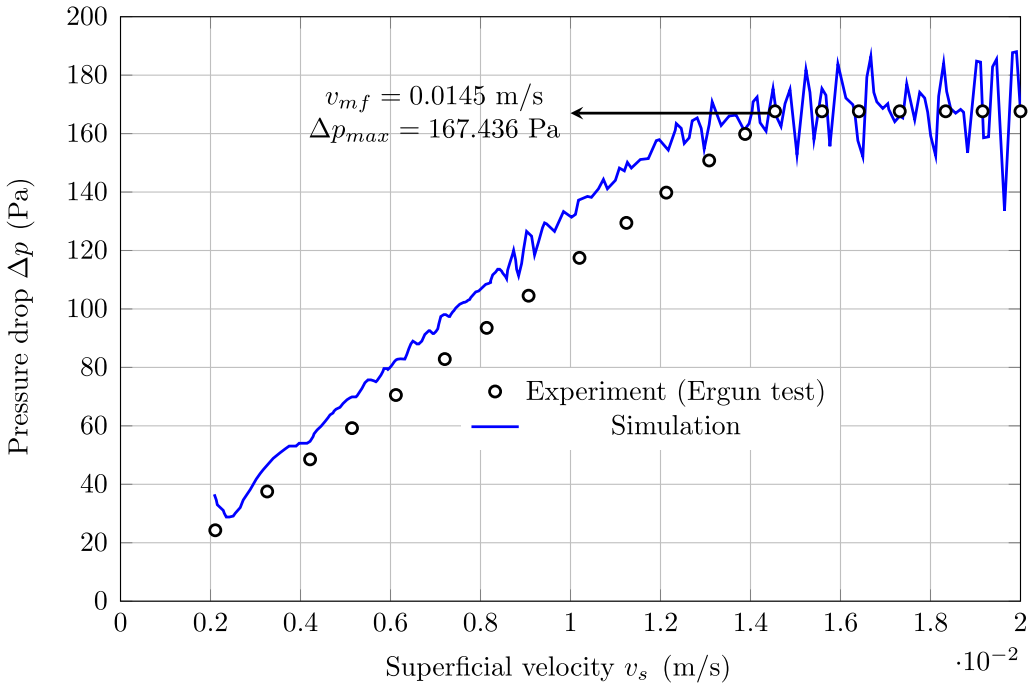

Fig. 4 Comparison of the pressure drop against the analytical solution provided by the Ergun equation

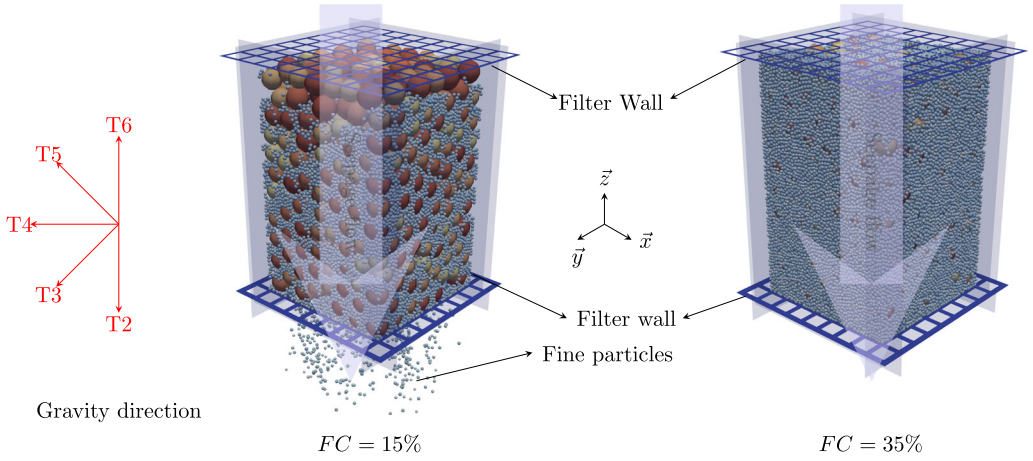

Fig. 5 Model setup

rigid walls, where either stress or strain control can be applied. The CFD domain has the same length and width but has an extra height of 8 mm, ensuring that it entirely covers the DEM domain. The boundary condition of the fluid is considered to be a one-way flow, which means that the fluid flows in from the top and flows out from the bottom. The surrounding surfaces are non-permeable and non-slip boundaries.

The soil particles are considered to be perfect spheres. The friction coefficient between particles is considered, whereas the effects of angularity are not considered in this study but will be investigated in a forthcoming study. The selection of Young's modulus in the DEM is a preparatory step for the simulation due to its importance in investigating the material's role in determining the time step of the DEM and to determine the particle overlapping. In the literature, a wide range (from 10^6 Pa to 10^{10} Pa) for Young's modulus has been adopted in numerical simulations to study sand behavior [11, 60, 68–71]. A smaller magnitude of Young's modulus allows for a larger time step, which can considerably save computational resources. Moreover, it has been found that a smaller magnitude of Young's modulus does not appreciably affect the physical response of the particulate system [3]. Thus, a magnitude of 10^9 Pa is selected for Young's modulus in this study, which ensures that the particle overlap is small enough (less than 2%). Other parameters used in this study are reported in Table 1.

Studies have shown that gap-graded soils are more prone to suffusion [33, 44], which may be a result of defects in construction or substandard procedures in soil mixing leading to a gap in certain grain sizes. Therefore, a gap-graded soil was chosen in this study. The soil mixtures are composed of fine particles with a radius of $d_{50} = 0.155$ mm and coarse particles with a radius of $D_{50} = 0.931$ mm. For internal instability problems, the index ratio D_{15}/d_{85} [43], based on splitting the gradation to distinguish between D_{15} of the coarse fraction and d_{85} of the finer fraction, was considered as the criterion. If $D_{15}/d_{85} < 4$, the soil is deemed internally stable. [13] experimentally demonstrated that a soil with a D_{15}/d_{85} ratio close to 4 appears stable, whereas a soil with $D_{15}/d_{85} \approx 7$ exhibits

Table 1 Parameters adopted in internal erosion process and mechanical behavior simulations

Parameter	Value	Unit
Particles		
Particle number	25240 or 58004	
Particle density	2630	kg/m^3
Young's modulus	1.5×10^9	Pa
Friction coefficient	0.25	
Restitution coefficient	0.5	
Time step	1×10^{-7}	
Diameter	0.131 $\sim$1	mm
Poisson's ratio	0.3	
Hole size of filter wall	0.65×0.65	mm^2
Walls		
Young's modulus	1.5×10^{10}	Pa
Friction coefficient	0.25	
Restitution coefficient	0.5	
Fluid		
Cell size	1×1×1	mm^3
Fluid density	1000	kg/m^3
Viscosity	1×10^{-6}	m^2/s
Hydraulic gradient difference	0.2	
Time step	1×10^{-4}	
Global setting		
Coupling time step	1×10^{-4}	
Gravitational acceleration	9.8	m/s^2

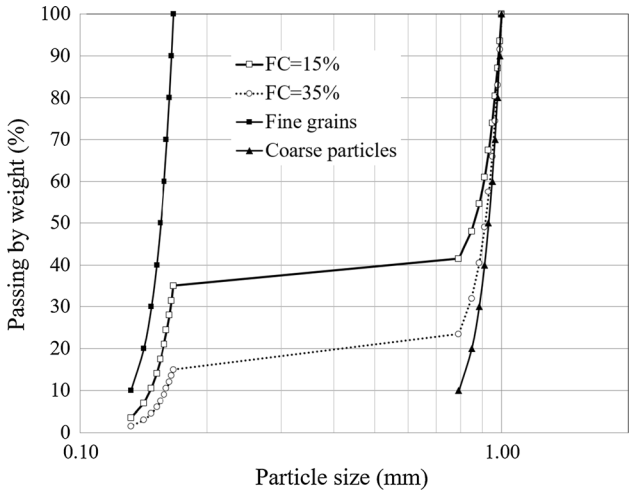

Fig. 6 Initial grain size distribution of samples

internal instability at a relatively low hydraulic gradient. Thus, the grain size distribution (GSD) shown in Fig. 6 with a ratio $D_{15}/d_{85} = 6$ was selected in this study.

As many experimental and DEM studies on suffusion [19, 20, 23, 37], the FC is a significant factor regarding the GSD for a given granular packing. In this study, two representative samples with different FCs are considered: FC=15% and FC=35%. In addition, to make the numerical results of two FCs comparable, the same relative density ($D_r = 60\%$) and sample size for different FCs are maintained. The relative density (D_r) is defined as follows:

$$D_r = \frac{e_{max} - e_0}{e_{max} - e_{min}}, \tag{7}$$

where e_{min} and e_{max} are the minimum and maximum void ratios for a given GSD, respectively. e_0 is the initial void ratio of the sample.

The method for determining the maximum and minimum void ratios follows [35]. By varying the generation porosity and interparticle friction, the maximum void ratio e_{max} (0.595 for FC=15% and 0.512 for FC=35%) and minimum void ratio e_{min} (0.363 for FC=15% and 0.271 for FC=35%) are obtained. The corresponding initial void ratios for FC=15% and 35% are 0.455 and 0.367, respectively.

3.2 Test program for suffusion

Suffusion may occur in many places in geotechnical structures or slopes, leading to uncertainty in the seepage direction. Different seepage directions result in different erosion consequences, particularly when the gravitational field direction is opposite to the seepage direction. In this study, the numerical simulations consist of four stages:

1. Stage 1: Sample generation. Particles are randomly generated (without any overlap) in a cuboid region slightly larger than the sample size, and then, the positions of the rigid walls are adjusted until the sample reaches the desired initial void ratio. Both the coupling calculation and gravity are switched off during this stage to ensure initial uniformity. The uniformity of the sample can also be numerically verified (blue histogram in Fig. 8).
2. Stage 2: Coupling balance. The coupling calculation and gravity (if it is considered) are switched on. The bottom and top walls are changed to filter walls. The hole size of the filter wall is 0.65 mm, which is smaller than the smallest diameter of the coarse particles but larger than the largest diameter of the fine particles. During this stage, the hydraulic gradient is kept at zero.
3. Stage 3: Suffusion test. This stage lasts for 50 s. In the first 5 s, the hydraulic gradient remains at zero; it is then increased to 0.2 and held at this value until the end of this stage. It should be noted that the confining pressures on the samples during the suffusion tests are kept at 100 kPa. The effect of the confining pressure is not investigated in this study.
4. Stage 4: Drained triaxial test. To analyze the mechanical consequences, the eroded or not eroded (i.e., underwent stage 3 or not) samples are both preserved. The conventional drained triaxial tests are conducted with three confining stresses of 100 kPa, 200 kPa and 400 kPa. Both gravity and seepage force are ignored in this stage. An axial strain of up to 40% is applied to ensure that all the samples reach the critical state.

A series of numerical tests were conducted to investigate the effects of different flow directions. For comparison purposes, a reference case was first considered in which the erosion process was conducted without the gravitational field. In addition, cases with an angle between the gravitational field direction and the seepage direction defined as α_g varying from 0° to 180° were conducted. Specifically, the flow direction is always vertical, but the direction of gravity is changed to achieve different angles. Two FCs (15%, 35%) were considered for each case. A summary of all the cases is reported in Table 2.

4 Numerical results and discussion

4.1 Detachment, transportation and clogging of fine particles

Figure 7 shows the evolution of the cumulative eroded mass ($M_e = \frac{\text{mass of eroded fines}}{\text{mass of total fines}}$) versus simulation time t for three selected gravity conditions: without gravity (T1),

Table 2 Summary of the internal erosion test program

Test	Gravity	α_g	FC(%)
T1-N-FC15	No	None	15
T2-Y0-FC15	Yes	0°	15
T3-Y45-FC15	Yes	45°	15
T4-Y90-FC15	Yes	90°	15
T5-Y135-FC15	Yes	135°	15
T6-Y180-FC15	Yes	180°	15
T1-N-FC35	No	None	35
T2-Y0-FC35	Yes	0°	35
T3-Y45-FC35	Yes	45°	35
T4-Y90-FC35	Yes	90°	35
T5-Y135-FC35	Yes	135°	35
T6-Y180-FC35	Yes	180°	35

with positive gravity (T2) and with negative gravity (T6). We first note that no loss of fine particles was observed in all tests during the first 5 s, indicating that the samples had reached equilibrium in stage 2. When the hydraulic gradient is applied, the fine particle loss of T2-Y0-FC15 is faster than that of T1-N-FC15 at the beginning but reaches a lower ultimate value of $M_{eu} = 26.81\%$, whereas T6-Y180-FC15 maintains a low value of $M_{eu} = 11.44\%$. A similar tendency is found in FC=35% samples, except that the M_{eu} of T2-Y0-FC35 reaches the value of 45.6%. By comparing the results of $\alpha_g = 0°$ and 180°, we also note that the direction of gravity has a significant influence on the erosion process. T2-Y0-FC15 and T2-Y0-FC35 reach a greater M_{eu} because the gravity direction is the same as the flow direction. However, fine particles are difficult to erode in T6-Y180-FC15 and T6-Y180-FC35 because the seepage force needs to overcome the gravitational force. For T1-N-FC15 and T1-N-FC35, the fine particles are eroded away from the coarse matrix continuously at a constant flow rate. In total, 41.11% and 15.79% of fines are eroded from the FC=15% and 35% samples, respectively. It is noted that the ultimate eroded mass M_{eu} of the FC=15% sample is much larger than that of the FC=35% sample, which is because the effective stresses are mainly transferred by the coarse particles in FC=15% samples. In contrast, in FC=35% samples, these stresses are transferred by the fine particles. T1 tests are necessary because the contact force between particles only stems from the confining pressures without considering the influence of gravity. Thus, under the same magnitude of the hydraulic gradient, the difference between T1-N-FC15 and T1-N-FC35 also highlights that the contact forces in the former are lower than those in the latter, which requires a stronger hydraulic force for detachment.

To investigate the fine particle detachment, transportation and clogging, the number of fine particles (N_{fc}) is classified as a distribution along the flow direction (Z position, x_z) both before and after erosion for cases T1, T2 and T6. As shown in Fig. 8, fine particles show a relatively homogeneous distribution before erosion (plotted in blue) for both FC samples due to the isotropic confining phase during sample preparation. However, after the erosion tests are performed, the fine particle distributions (plotted in red) are no longer homogeneous and instead show a triangle-like distribution. With an increase in x_z, increasingly more fines are clogged. This result could be interpreted as follows: the longer the distance that the fines need to be transported, the greater the possibility for them to be clogged. It is worth noting that the volumetric change of the FC=35% sample is larger than that of the FC=15% sample because considerable fine particles are eroded, while a constant confining pressure is maintained during the erosion process. As mentioned before, the force transmission in FC=35% is mainly through fine particles. Therefore, when the top-side fine particles are detached,

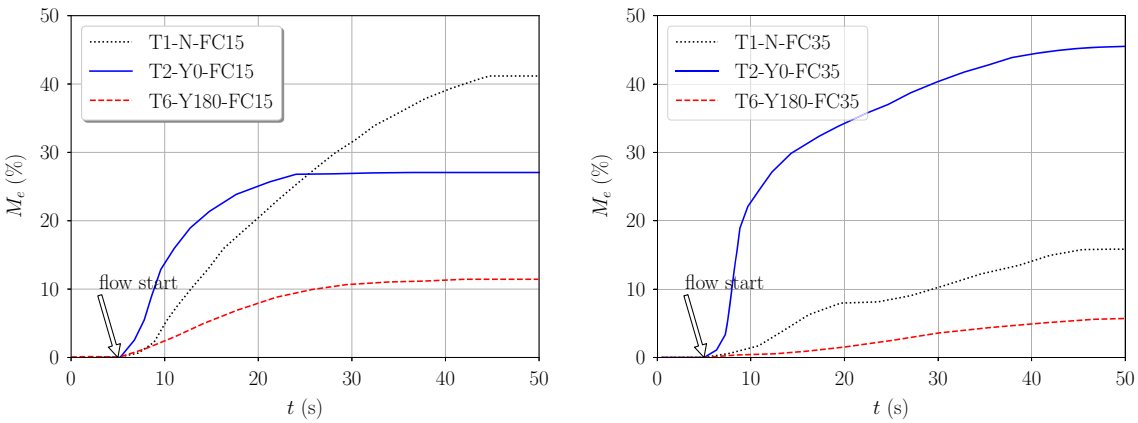

(a) FC=15% **(b)** FC=35%

Fig. 7 Evolution of cumulative eroded mass (M_e) of fines for three cases: without gravity, with positive gravity and with negative gravity

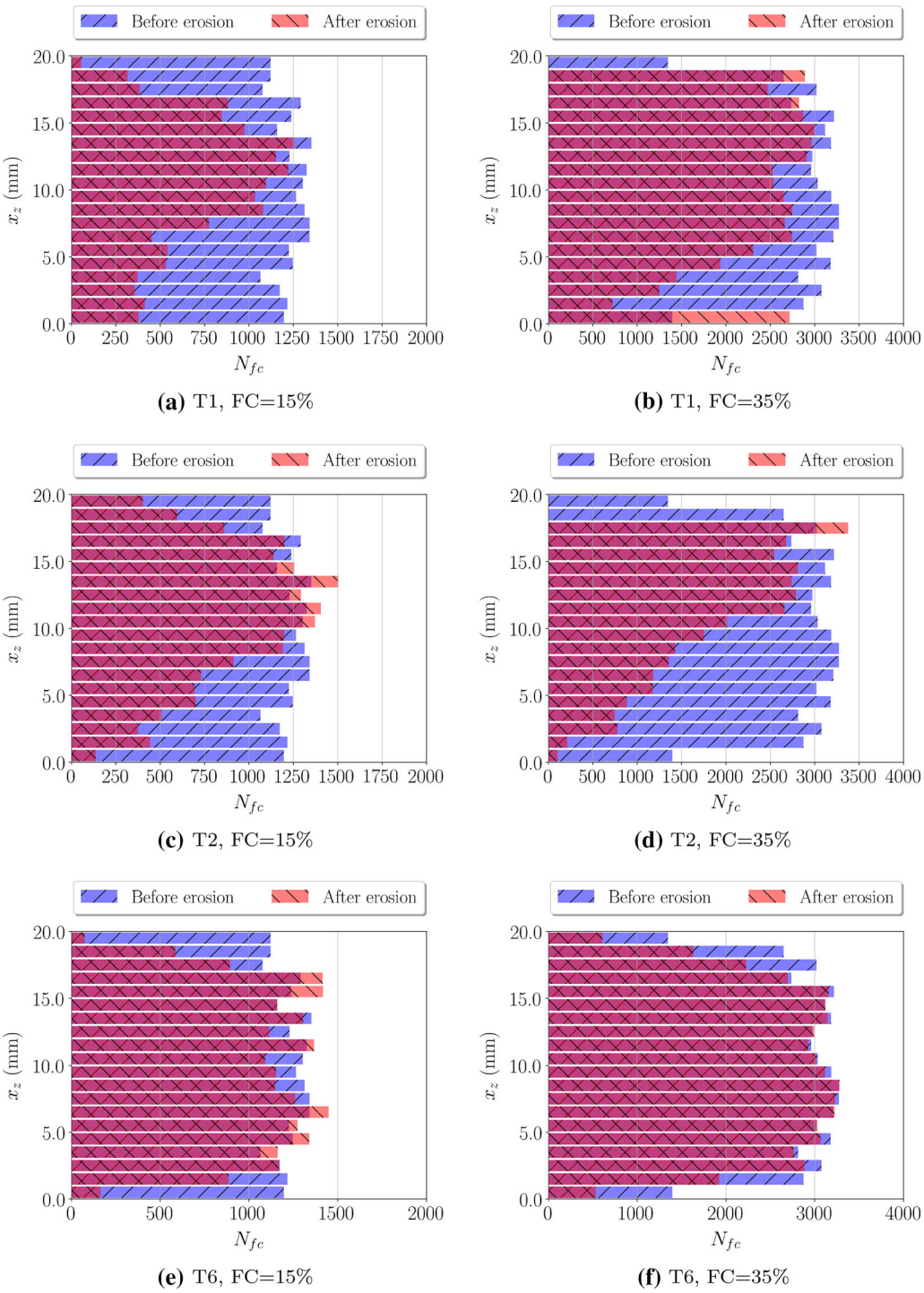

Fig. 8 Comparison of fine particle (N_{fc}) distribution along Z position (x_z) at the state before and after erosion, without gravity (T1), with positive gravity (T2) and with negative gravity (T6)

particle rearrangement occurs, resulting in the compression of FC=35% samples, whereas this effect is not distinguished in the FC=15% sample. Although a large portion of fines are washed away from the top side, there are still a few fines remaining because the coarse particles carry the external forces, leaving void space for fine particles, as shown in Fig. 8a and c. Since fewer fine particles in case T6 are eroded, the fine particle distribution of tests T6-Y180-FC15 and T6-Y180-FC35 does not change significantly. Only a few fine particles around the top and bottom

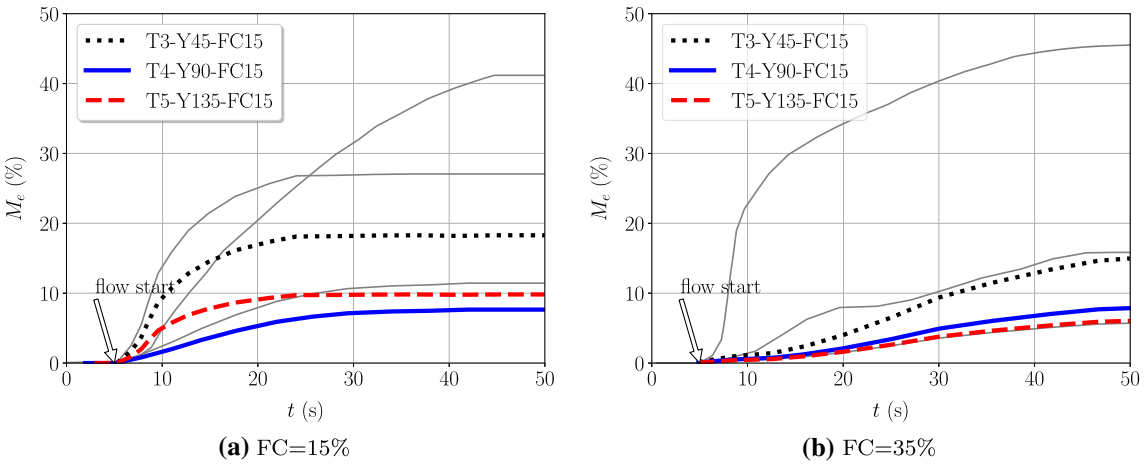

Fig. 9 Evolution of cumulative eroded mass (M_e) of fines for T3, T4 and T5

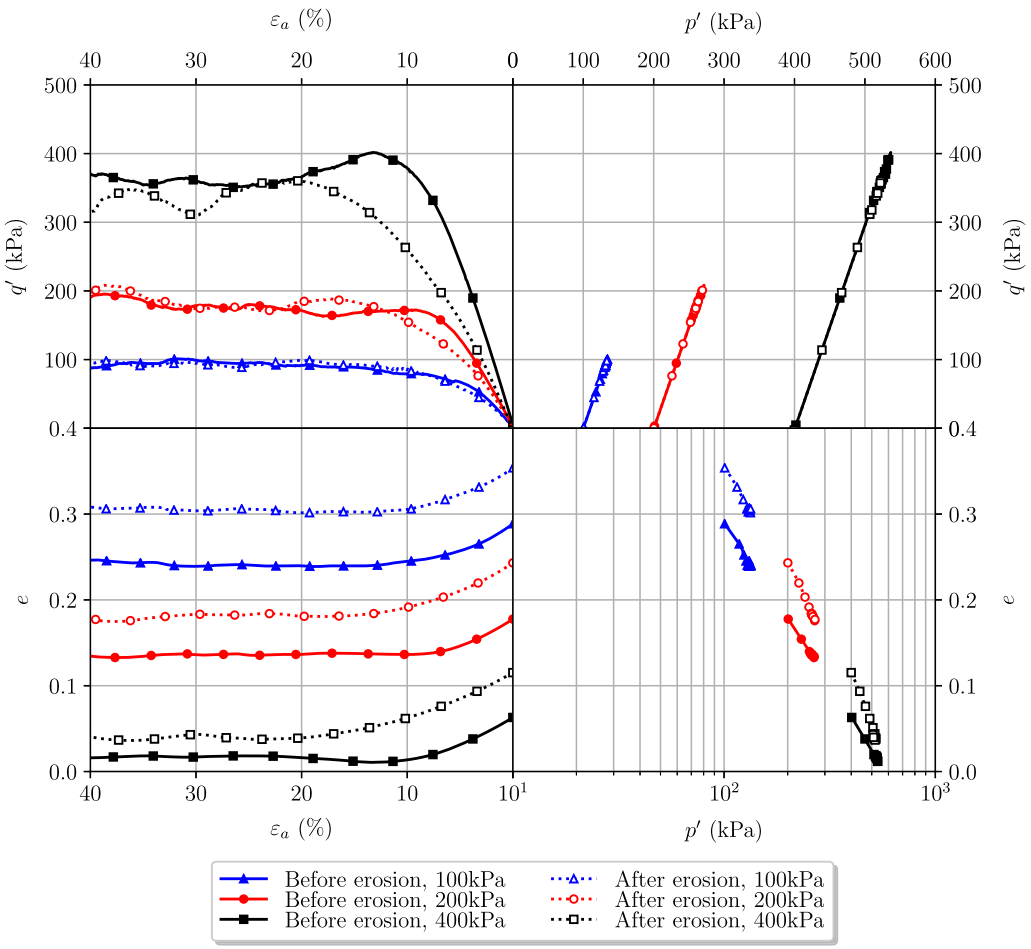

Fig. 10 Comparison of drained triaxial tests with and without erosion of T1-N-FC15

are eroded, indicating that most fine particles are not detached. A comparison between the results of FC = 15% and FC = 35% illustrates that the transport of fines in the FC = 15% sample is easier than that in the 35% sample because this mitigation of fine particles needs a void channel between coarse particles, and the void in the FC = 15% sample is generally larger than that in the 35% sample.

Figure 9 shows the evolution of the cumulative eroded mass (M_e) versus simulation time t for the other three

cases: T3, T4 and T5. It is worth noting that the curves (plotted in gray) shown in Fig. 7 are retained in this figure for reference. The greatest difference between FC = 15% and FC = 35% is that the former starts to lose fine particles when the seepage flow starts, while the latter lags behind for a while. This outcome occurs because there are more free fine particles in FC = 15% samples than in FC = 35% samples. When seepage flow starts, these free fine particles are the first to be washed away. However, the fine particles need to be detached under the drag force before they can be washed away in FC=35% samples. Another difference is that the ultimate eroded mass (M_e^u) decreases with the increasing angle α_g in FC = 35%, and minimal fine particle loss occurs when the gravity direction is opposite to the flow direction (T6-Y180-FC35). However, this also happens when the gravity is perpendicular to the flow direction in T4-Y90-FC15. The reason for this phenomenon is that the perpendicular gravity tends to push some detached fine particles to the side that contacts coarse particles away from the pipe by voids among coarse particles along the flow direction. Thus, the fine particles become clogged more easily in the FC = 15% sample, whereas the FC = 35% sample is different because of its lower number of detached fine particles.

4.2 Consequent mechanical responses

With the erosion of large amounts of fines, a metastable structure might be formed, which easily triggers the rearrangement of particles into a stable packing. Consequently, a volumetric deformation with a change in the void ratio takes place, and the mechanical responses of the soil may change significantly. For example, Figs. 10 and 11 show the comparison of the mechanical responses of T1-N-FC15 and T1-N-FC35 samples before and after erosion. The triaxial loading tests at three different confining pressures (100 kPa, 200 kPa and 400 kPa) are performed, where ε_a is the axial strain along the Z-axis; p' is the effective mean stress; q' is the deviatoric stress; and e is the void ratio. For the eroded and non-eroded samples, three major differences are observed:

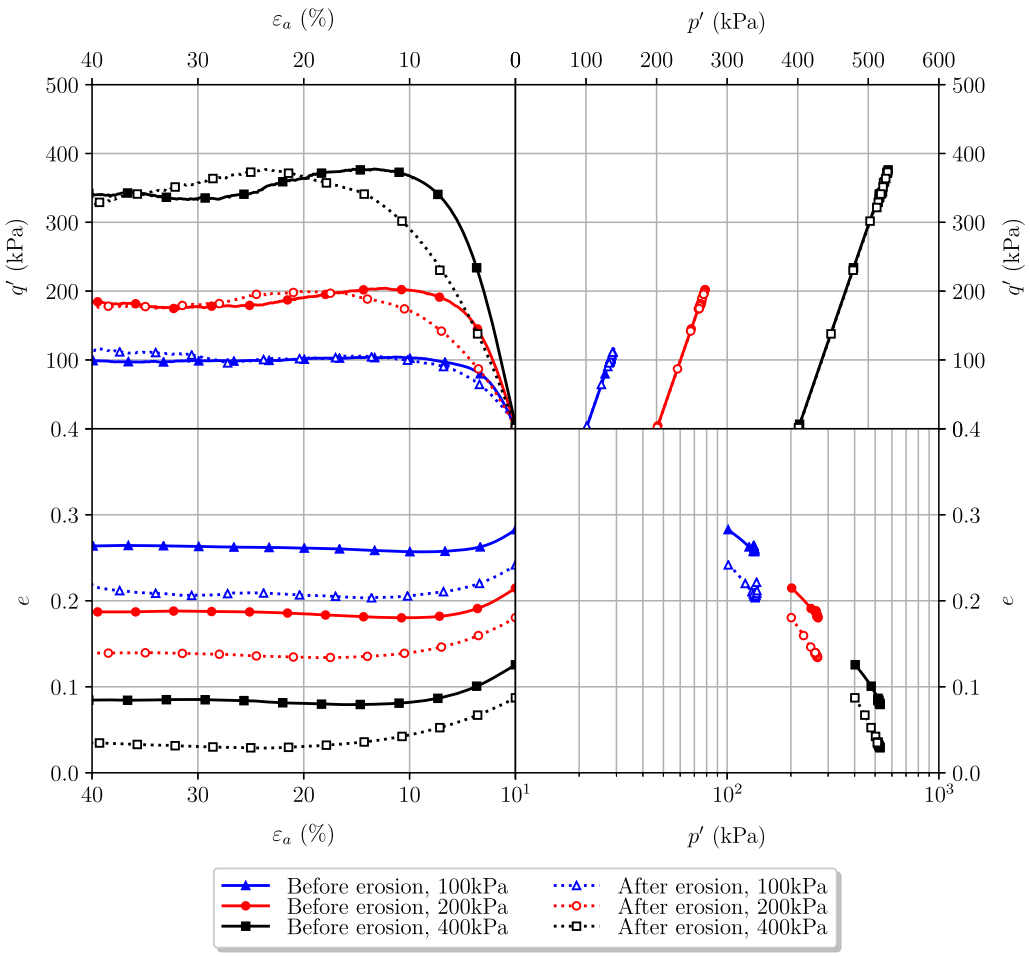

Fig. 11 Comparison of drained triaxial tests with and without erosion of T1-N-FC35

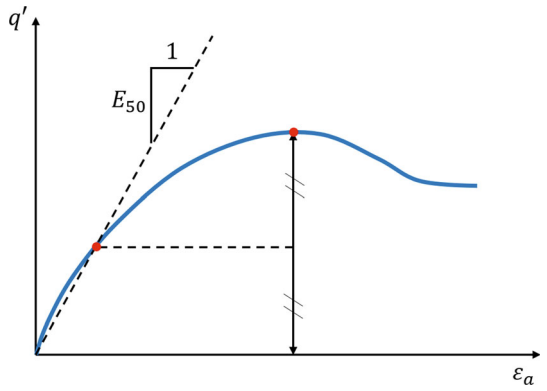

Fig. 12 Definition of E_{50}

1. A reduction in soil stiffness is observed, as shown in the top-left subfigure. Due to the nonlinearity of the soil (even at the beginning of loading), a stiffness parameter E_{50} was introduced, which is defined as the secant modulus corresponding to half of the peak stress (depicted in Fig. 12).

Table 3 Summary of numerical results after erosion

Test	$M_{eu}(\%)$	Δe	e_{ref}
T1-N-FC15	41.11	0.061	0.354
T2-Y0-FC15	26.81	0.041	0.337
T3-Y45-FC15	18.29	0.024	0.322
T4-Y90-FC15	7.65	0.003	0.304
T5-Y135-FC15	9.82	0.005	0.287
T6-Y180-FC15	11.44	0.012	0.290
T1-N-FC35	15.79	0.018	0.242
T2-Y0-FC35	45.60	0.049	0.232
T3-Y45-FC35	14.98	0.026	0.241
T4-Y90-FC35	7.86	0.015	0.263
T5-Y135-FC35	6.04	0.012	0.269
T6-Y180-FC35	5.70	0.015	0.269

2. The change in void ratio shown in the bottom-left subfigure is mainly due to the erosion of large amounts of fines. The change in the void ratio during erosion is denoted as Δe.

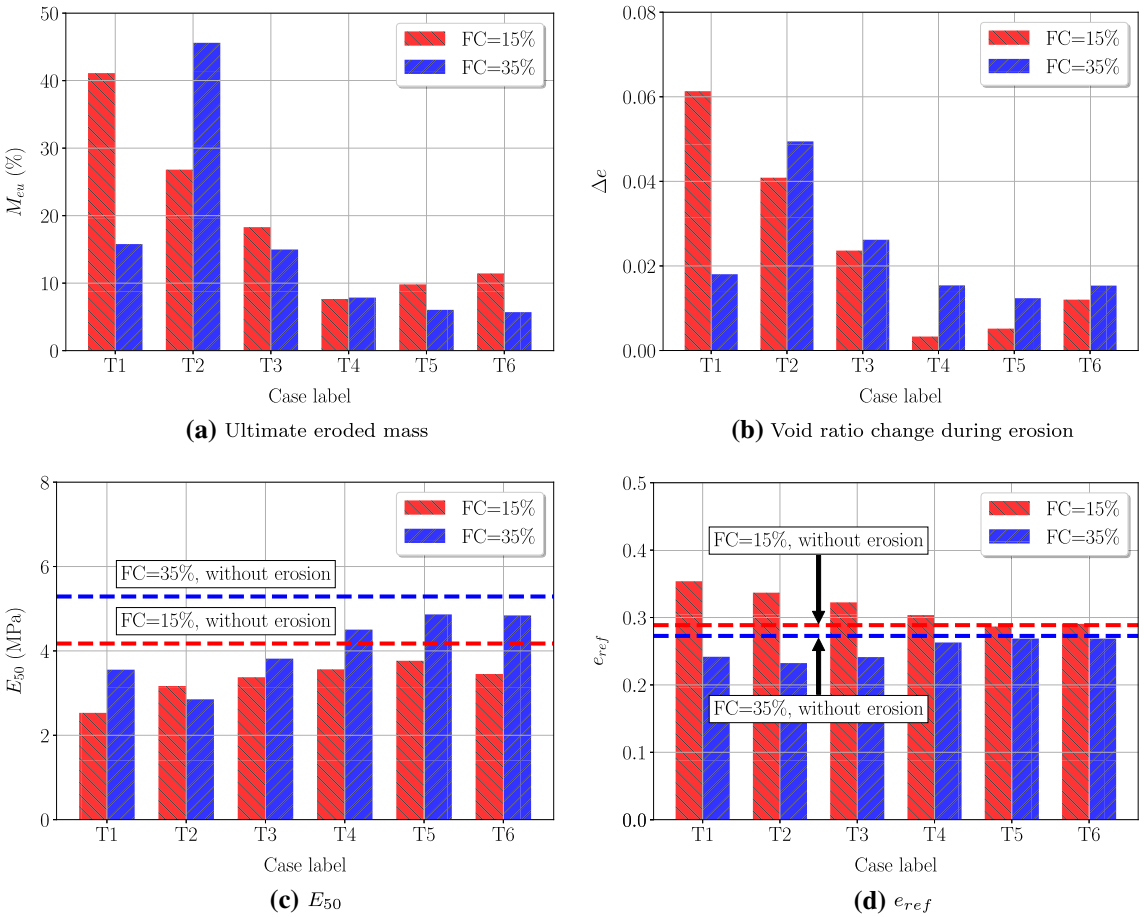

(a) Ultimate eroded mass

(b) Void ratio change during erosion

(c) E_{50}

(d) e_{ref}

Fig. 13 Determine the effect of seepage direction for different cases with both FC = 15% and 35%: **a** ultimate eroded mass; **b** void ratio change during erosion; **c** E_{50} at 400 kPa of confining pressures; **d** e_{ref} with $p'_{ref} = 100$ kPa

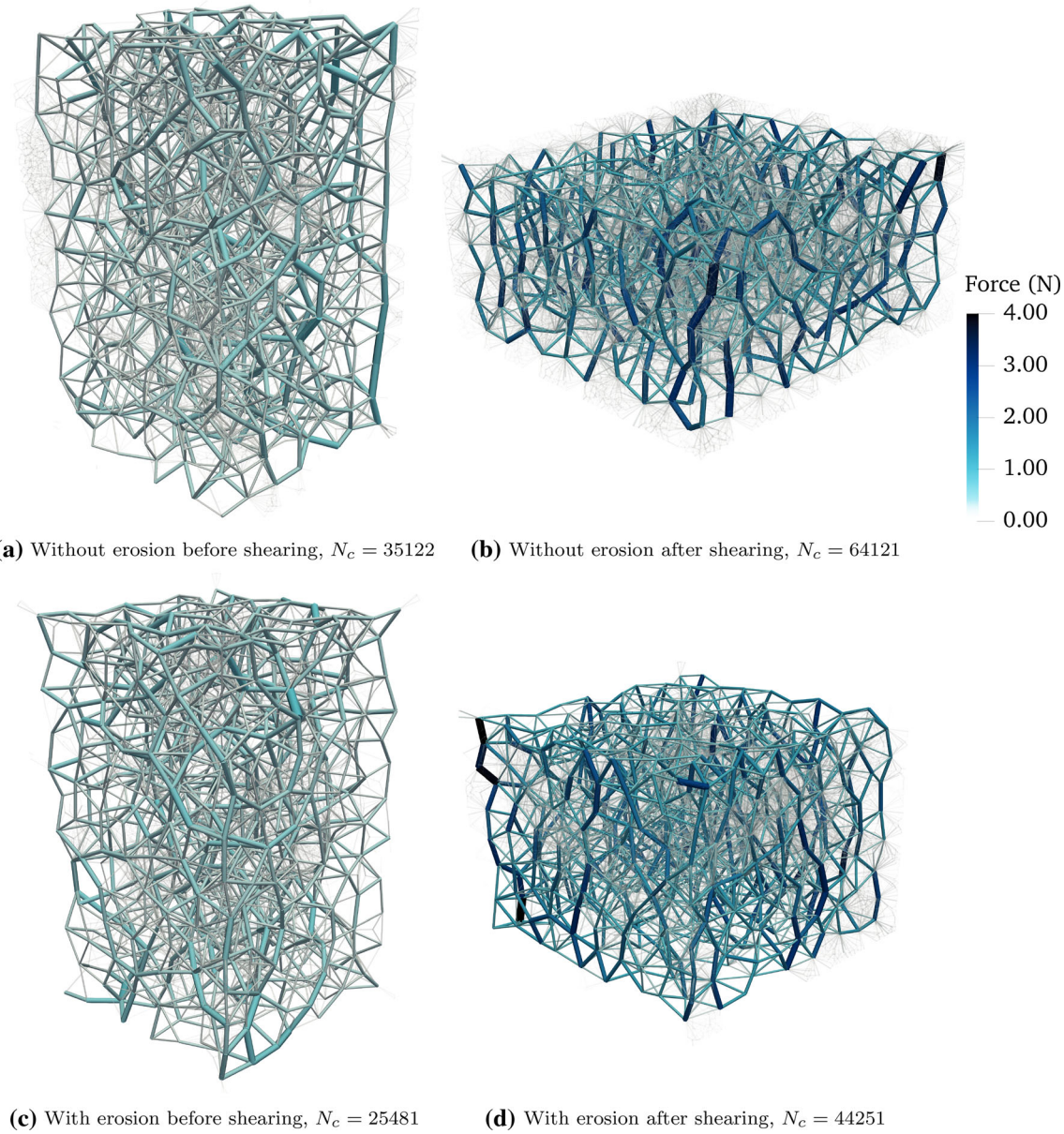

(a) Without erosion before shearing, $N_c = 35122$ **(b)** Without erosion after shearing, $N_c = 64121$

(c) With erosion before shearing, $N_c = 25481$ **(d)** With erosion after shearing, $N_c = 44251$

Fig. 14 Force-chain network for case T1-N-FC15 confined at 400 kPa

3. The change in the critical state line (CSL) is also observed in the bottom-right subfigure. According to [30, 35, 36, 62, 63], changes in the grading of GSD will result in changes in the position of the CSL. Note that the critical void ratio e_c is a function of the mean effective stress p'.

A simple linear relation for the CSL was adopted in the $e - \ln p'$ plane according to the results:

$$e_c = e_{ref} - \lambda \ln \frac{p'}{p'_{ref}}, \tag{8}$$

where e_{ref} and p'_{ref} determine a reference point of the critical state in the $e - \ln p'$ plane, and λ denotes the slope of the CSL. Thus, the CSL can be described by the two parameters e_{ref} and λ when p'_{ref} is assigned (p'_{ref} = 100 kPa in this study).

As listed in Table 2, the angle between the seepage and gravity directions is characterized by α_g, which varies from 0° to 180°. Figure 13 shows the comparison of results for different cases with the two different FCs. Figure 13a shows the results of the ultimate eroded mass. For both FCs, M_{eu} decreases as α_g increases, and the M_{eu} of the FC = 35% samples decreases faster than that of the FC = 15% samples. It is worth noting that a significant difference can be observed between FC=15% and 35% for T1, implying that fine particles in FC = 15% samples can

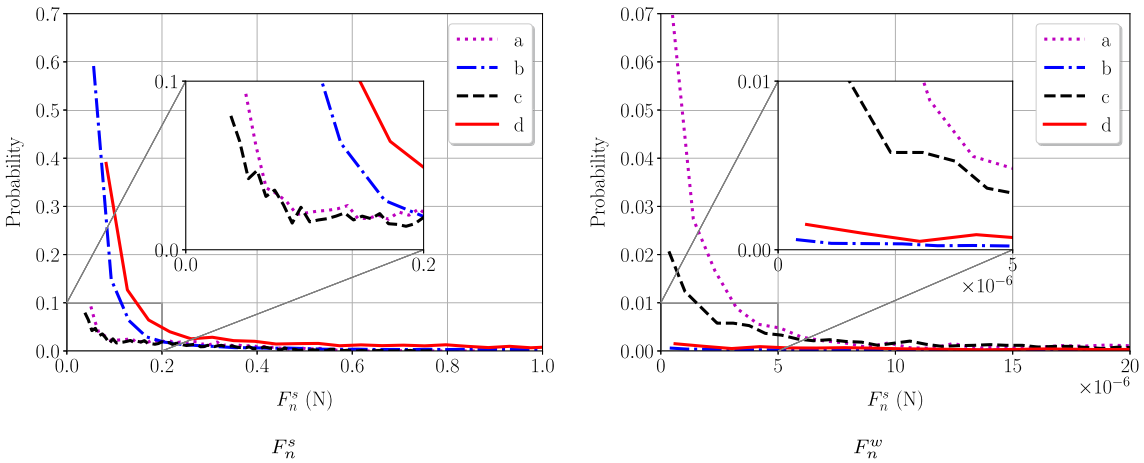

Fig. 15 Probability density function of strong ($F_n^s > \bar{F}_n$) and weak ($F_n^w < \bar{F}_n$), legend labels correspond to four states shown in Fig. 14: **a** Before erosion, $N_c = 35122$; **b** At critical state without erosion, $N_c = 64121$; **c** After erosion, $N_c = 25481$; (d) At critical state with erosion, $N_c = 44251$

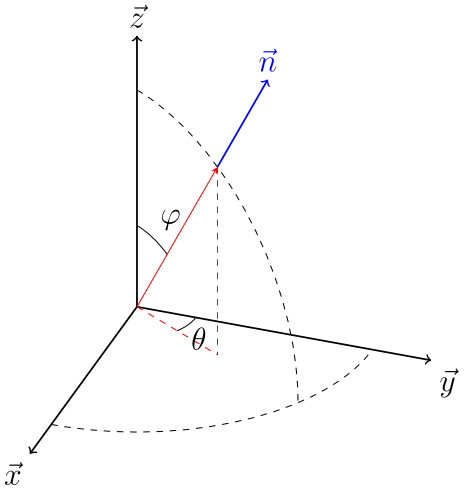

Fig. 16 Three-dimensional framework

more easily be eroded. Similar observations can be found in Fig. 13b, which shows the void ratio change during the erosion process for different cases. The two subfigures have a certain correlation, and the loss of fine particles increases the porosity, but it is also necessary to consider the volume change of the whole sample. Figure 13c summarizes the trends of E_{50} (for the definition, see details in Fig. 12) under different conditions. For comparison, the dashed line is obtained from the sample without erosion. It is observed that for all cases, E_{50} is reduced after the erosion process. The drag forces applied by the fluid flow cause some metastable force-chain buckling, leading to the reduction of E_{50}. Thus, the more fine particles that are lost, the more that E_{50} changes. Figure 13d illustrates the reference critical void ratio e_{ref} relating to the position of the CSL (see details in Eq. 8 when the slope $\lambda = 0.166$ remains almost the same). After the erosion process, the reference critical void ratio e_{ref} increases for the FC = 15% samples, while it decreases for the 35% samples. The numerical results after the erosion process are reported in Table 3.

4.3 Micromechanical analysis

The impact of suffusion not only is reflected macroscopically but also changes the soil structure microscopically. The analysis of the microstructure changes is also of great significance for studying suffusion mechanisms. Figure 14 shows the force-chain network for case T1-N-FC15 confined at 400 kPa in order to compare and analyze the influence of flow on the micromechanical aspect. For comparison purposes, four states are selected: (a) the state without erosion before shearing; (b) the state without erosion after shearing; (c) the state with erosion before shearing; and (d) the state with erosion after shearing. As shown in Fig. 14a and c, the force chains randomly distribute in the two samples, showing isotropic distribution due to having the same confining pressure of 400 kPa; however, the number of contacts N_c is reduced from 35122 to 25481 due to the detachment and transport of fine particles, which also implies that the erosion process leads to particle rearrangement. Moreover, after applying vertical loading until the critical state (as shown in Fig. 14b and d), the contact anisotropy is easily found; it is better illustrated in Fig. 15, which shows the probability density of strong (F_n^s greater than average) and weak (F_n^w less than average) normal contact forces, where the average normal contact force is denoted by $\bar{F}_n$. By comparing the results before shearing with and without erosion (states a and c), the proportion of F_n^s does not change significantly. However, the proportion of F_n^w decreases due to the seepage flow, which implies that the detachment of fine particles is

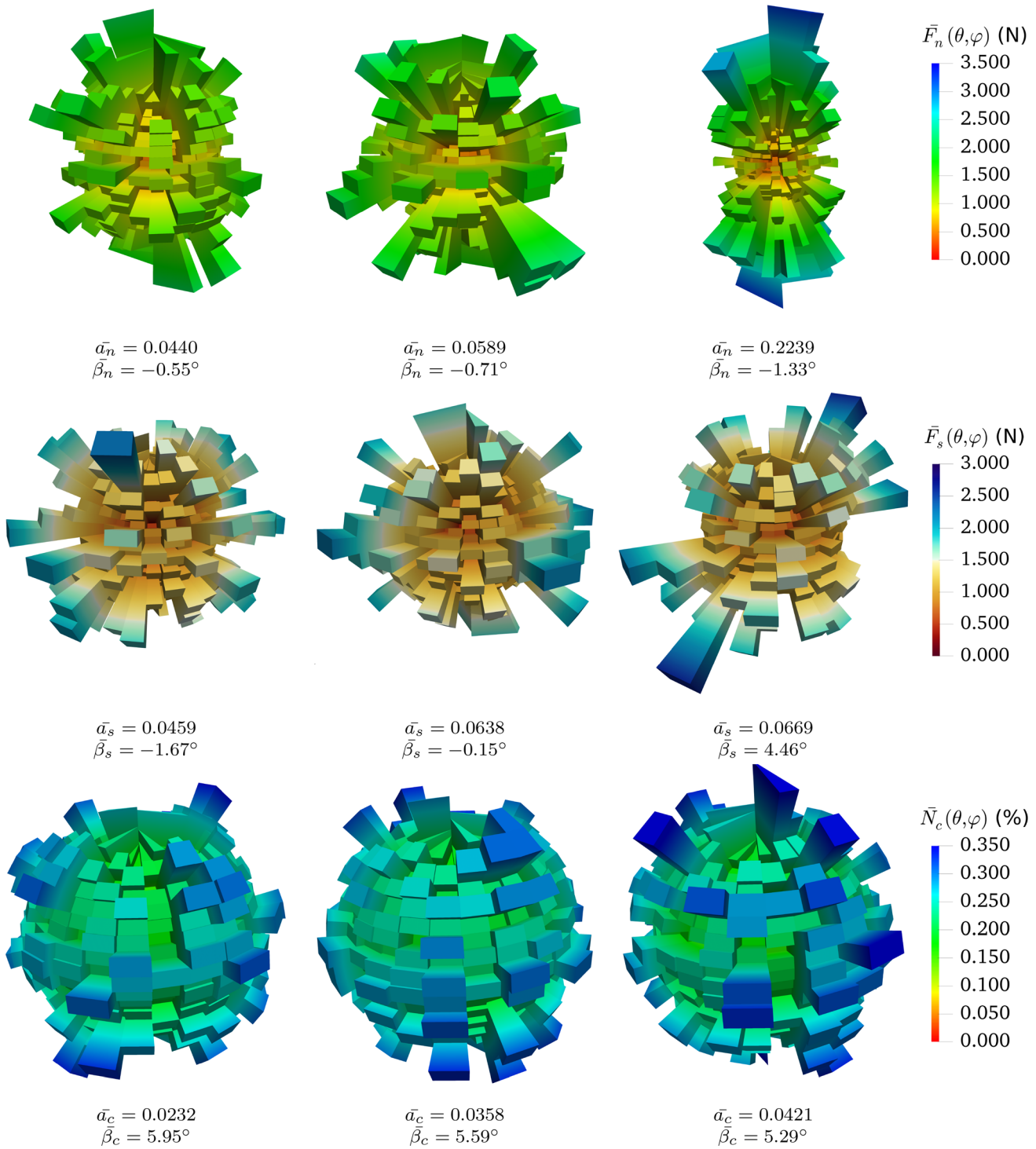

Fig. 17 Orientations of normalized microscopic contact information of T1-N-FC15, confined at 100 kPa, left column: without erosion before shearing; mid column: with erosion before shearing; right column: with erosion after shearing

involved mainly in weak force chains. Moreover, by comparing the results after shearing with and without erosion (states b and d), it is observed that the proportion of F_n^s for the latter is larger than for the former, which is because both N_c and the number of fine particles in the latter are less than those in the former, so fewer particles are required to sustain the same magnitude of confining pressure, thereby resulting in a higher proportion of F_n^s.

Furthermore, the contact information can be considered as a three-dimensional (3D) spatial distribution.

Considering a 3D framework, all spatial orientations can be expressed as a function of two angles θ and φ (similar to that in [57–59]), as depicted in Fig. 16. Thus, the contact orientations can be characterized by an angular distribution function $E(\theta, \varphi)$ defining the portion of contacts falling within an angular interval $(d\theta, d\varphi)$. Since the loading considered in this study is symmetric about the Z-axis, the influence of θ can be eliminated by averaging the distribution function as $\bar{E}(\varphi) = \frac{\int_0^{2\pi} E(\theta,\varphi)d\theta}{\int_0^{2\pi} d\theta}$. Since $\bar{E}(\varphi)$ along directions φ and $\varphi + \pi$ is physically equivalent, it can always be represented by a Fourier series containing even components. An adequate approximation for $\bar{E}(\varphi)$ can be obtained on the basis of the second Fourier components as follows:

$$\bar{E}(\varphi) = \frac{1}{2\pi}[1 + a\cos 2(\varphi - \beta)] \tag{9}$$

where a is a parameter defining the magnitude of the anisotropy (a_n for a normal contact force, a_s for a shear contact force, a_c for the contact number) and β defines the principal direction of the anisotropy (β_n for a normal contact force, β_s for a shear contact force, β_c for the contact number). When $a = 0$, the distribution is isotropic and $\bar{E}(\varphi) = 1/2\pi$, ensuring that $\int_0^{2\pi} \bar{E}(\varphi)d\varphi = 1$. Therefore, a and β can be computed as:

$$a = 2\sqrt{\left[\int_0^{2\pi} \bar{E}(\varphi)\cos 2\varphi d\varphi\right]^2 + \left[\int_0^{2\pi} \bar{E}(\varphi)\sin 2\varphi d\varphi\right]^2} \tag{10}$$

$$\beta = \frac{1}{2}\arctan\frac{\int_0^{2\pi} \bar{E}(\varphi)\sin 2\varphi d\varphi}{\int_0^{2\pi} \bar{E}(\varphi)\cos 2\varphi d\varphi} \tag{11}$$

As an example, Fig. 17 shows the orientations of the three kinds of microscopic contact information for T1-N-FC15. The first row shows a normalized normal contact force F_n, the second row displays a normalized shear contact force F_s, and the third row presents the percentage of the contact number N_c. By adopting Eqs. 10 and 11, the anisotropy coefficient and principal direction are obtained, respectively. It is worth noting that this study presents the analysis of conventional drained tests just for the mechanical consequences, since the initial fabric effect on the anisotropy of mechanical behavior of granular materials has been widely studied [61, 65].

From the results of the first and second columns, it can be stated that the suffusion process leads to an increase in $\bar{a}_n$, $\bar{a}_s$ and $\bar{a}_c$, indicating an increase in the anisotropy of the sample. However, due to symmetric conditions, the value of β does not change significantly. Subsequently, when triaxial loading is applied, it can be observed that the distributions of F_n and F_s exhibit noticeable changes.

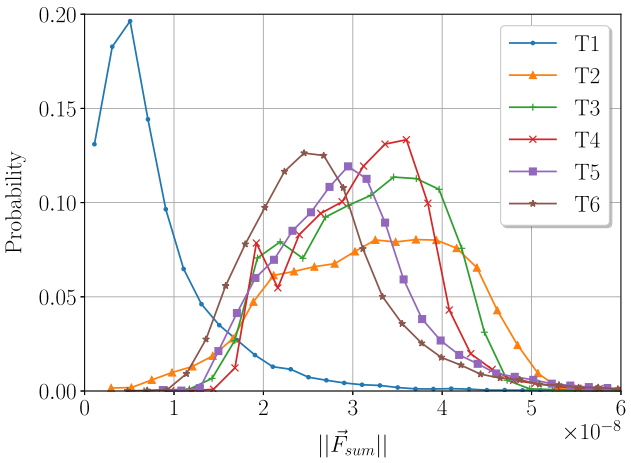

Fig. 18 Probability density of resultant force length $||\mathbf{F}_{sum}||$ applied on the fine particles, in FC=15% samples for different flow directions

In addition, the forces acting on the fines (during the erosion test) include the gravity force ($\mathbf{f}_g$), drag force ($\mathbf{f}_d$), normal contact force ($\mathbf{f}_n$), shear contact force ($\mathbf{f}_s$) and pressure gradient force ($\mathbf{f}_{\Delta p}$). Thus, the resultant force acting on one fine grain can be computed as:

$$\mathbf{F}_{sum} = \mathbf{f}_g + \mathbf{f}_d + \mathbf{f}_s + \mathbf{f}_n + \mathbf{f}_{\Delta p}. \tag{12}$$

Figure 18 shows the probability density of $||\mathbf{F}_{sum}||$ applied to the fine particles for the FC=15% samples. It is worth noting that $||\mathbf{F}_{sum}||$ reflects the possibility of fine particle detachment. As shown in the figure, the $||\mathbf{F}_{sum}||$ value of the peak positions for different cases decreases with an increase in the angle α_g. This figure gives an explanation of the influence of the change in seepage directions from a grain-scale point of view.

Figure 19 summarizes the anisotropy coefficients and directions of micromechanical distributions for all the cases. The results for the FC = 15% samples are plotted in red, while the results for FC = 35% are in blue. Three states are selected for presentation: before erosion, after erosion and at a critical state with respect to the states presented in Fig. 13. As shown in Fig. 19a and e, the first observation with regard to the evolution of a_n is that it shows a high correlation with a_c. For the FC = 15% group, the sample at the state before erosion shows the highest anisotropy. Then, when the erosion and triaxial tests are performed, a_n and a_c decrease. However, this effect is in contrast to that of the FC = 35% group. It should be noted that the anisotropy coefficients and directions presented here are different from the fine particle distribution in Fig. 8 because this is in terms of the contact orientations, not the positions. In general, the anisotropy of the shear force is more significant than that of the normal force and

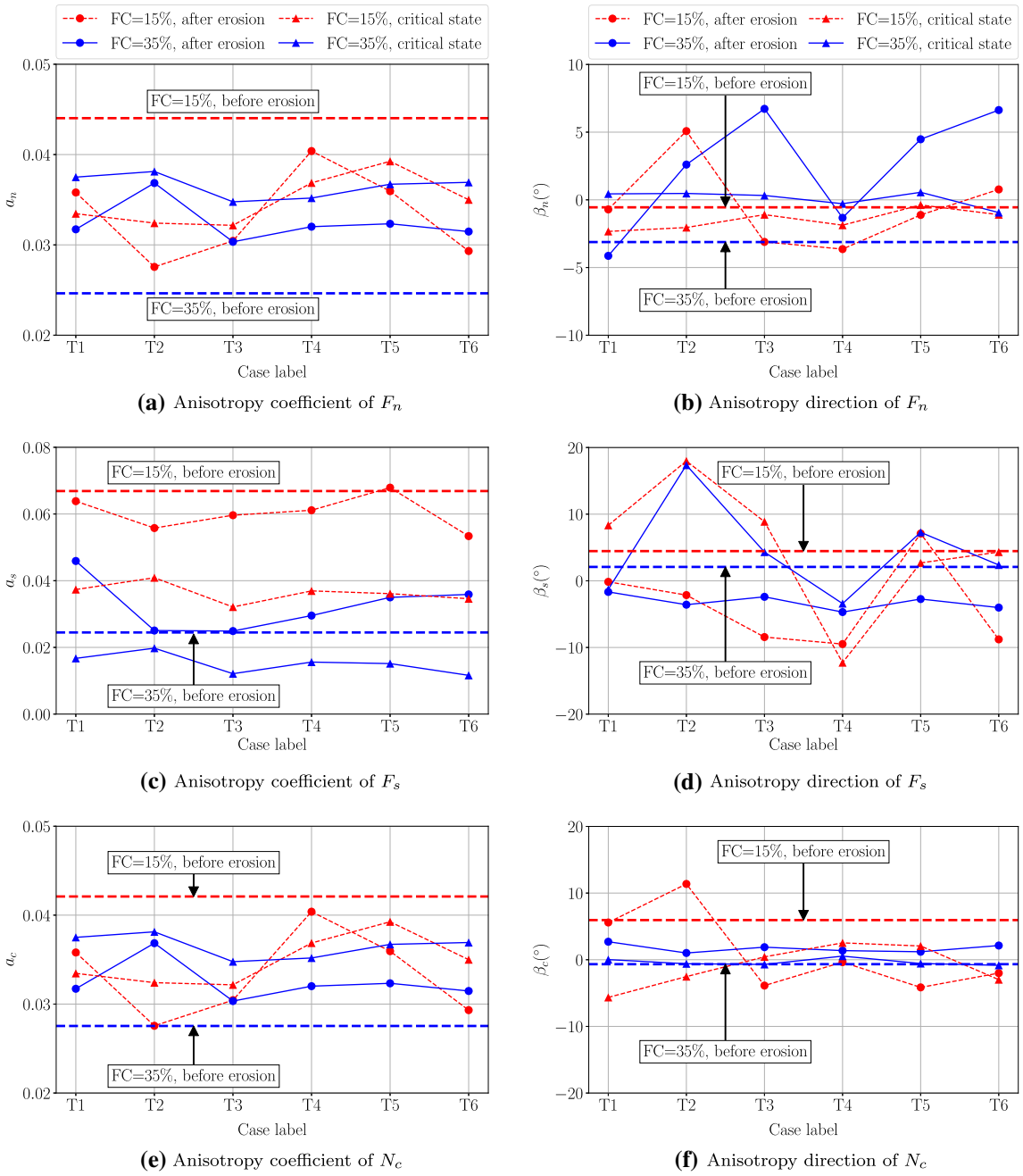

(a) Anisotropy coefficient of F_n

(b) Anisotropy direction of F_n

(c) Anisotropy coefficient of F_s

(d) Anisotropy direction of F_s

(e) Anisotropy coefficient of N_c

(f) Anisotropy direction of N_c

Fig. 19 Summary of anisotropy coefficients and directions of micromechanical orientations for different cases and FCs

contact number, which can be observed by the values of a_s, a_n and a_c, respectively. On the other hand, the evolution of β_n, β_s and β_c is based on the fluctuations of 0° due to the symmetric condition. It is noteworthy that the erosion process makes β_n, β_s and β_c move away from 0°, which means that a portion of the contact is lost, and the principal direction of the anisotropy is deviated. Moreover, after the triaxial loading applied, β_n, β_s and β_c become closer to 0°, indicating that the sample is compressed and new contacts are rebuilt.

4.4 Summary of micro- and macro-characteristics for erosion rule

Finally, together with all the macroscopic and microscopic characteristics of all cases, a general erosion rule with critical thresholds for the involved variables can be examined. Taking the erosion law of [52] as an example, the eroded mass rate can be expressed as follows:

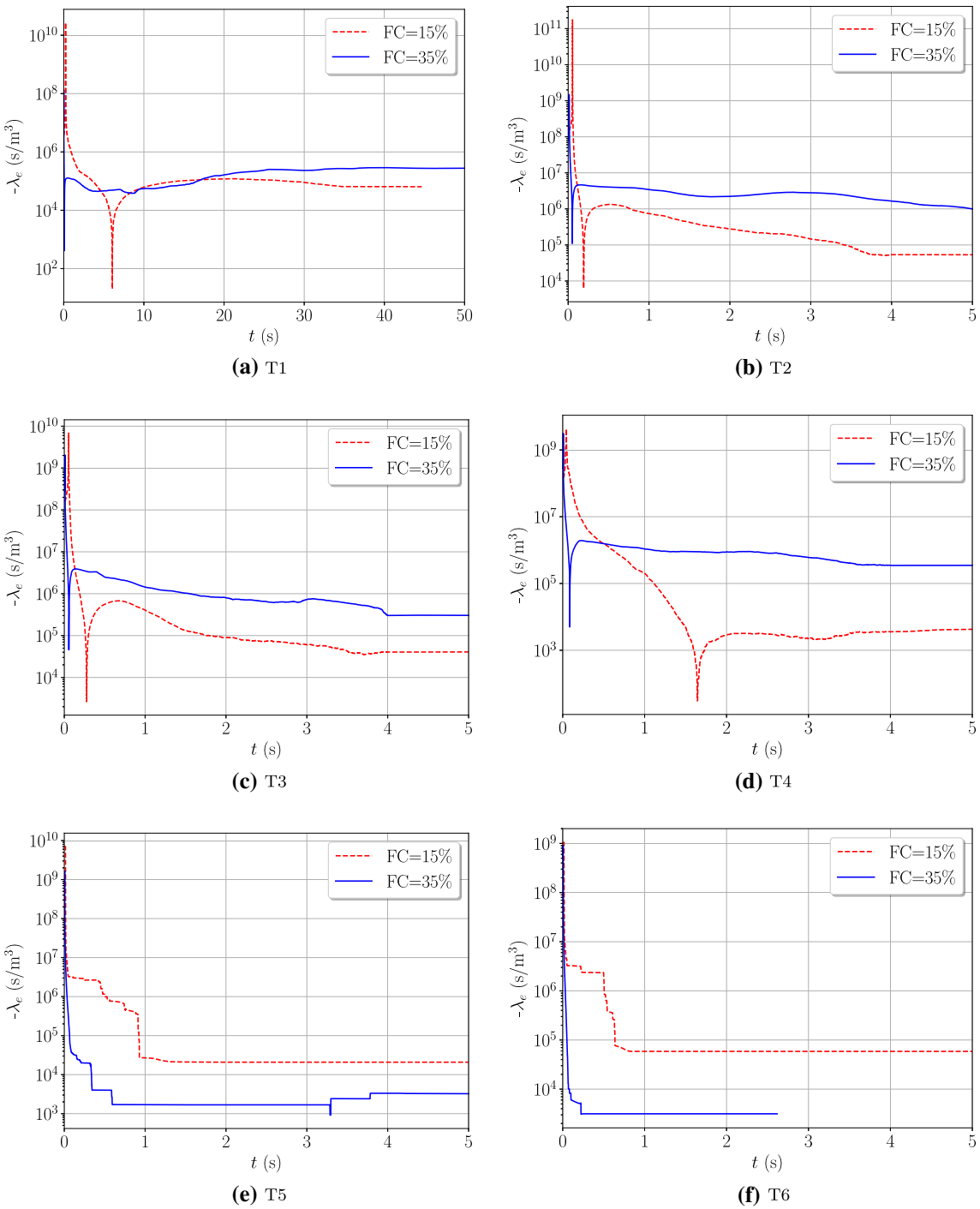

Fig. 20 Summary of λ_e for different cases and FCs

$$\hat{n}_e = -\lambda_e(1-\phi)(f_c - f_{c\infty})|q_w|, \tag{13}$$

where f_c is the fines content and $f_{c\infty}$ is the ultimate fines content after a long seepage period; λ_e is the material parameter; q_w denotes the volume discharge rate (the volume of flow through the unit cross-sectional area per unit time); ϕ is the porosity; and $\hat{n}_e$ is the eroded mass rate. Thus, Eq. 13 can be rewritten as:

$$\lambda_e = \frac{-\hat{n}_e}{(1-\phi)(f_c - f_{c\infty})|q_w|} \tag{14}$$

According to Equation 14, the variables used to calculate λ_e can be measured from the CFDEM simulations. Figure 20 shows the evolution of $-\lambda_e$ versus time for different cases and FCs. As erosion progresses, the value of λ_e gradually stabilizes. The maximum, minimum and mean

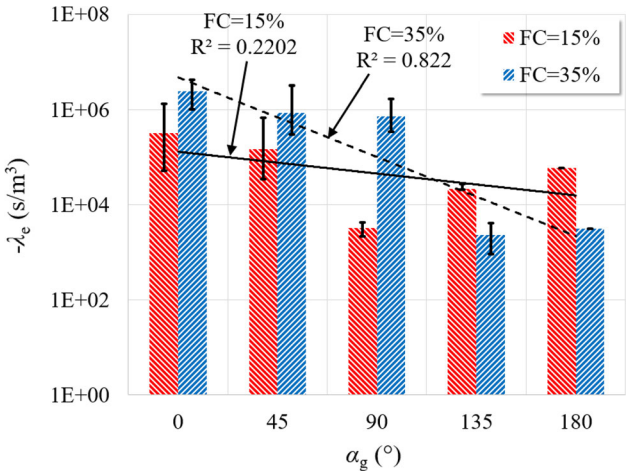

Fig. 21 Error bar and exponential regression of λ_e for different cases and FCs

values are summarized in Fig. 21. The λ_e is obviously not constant, indicating that more factors need to be considered in the erosion law. That is, it may not be suitable to use the quantity $f_c - f_{c\infty}$ accounting for the changing in the fines content since this linear relationship cannot express the two totally different force-chain transmissions that exist in samples with different initial fines contents. Other influencing factors (including hydraulic gradient, confining pressures and interparticle friction angles, etc.) might also lead to the nonlinear λ_e. In addition to these reasons, it can be clearly seen that λ_e is highly dependent on the angle between the gravity and seepage directions, which should be considered in proposing the erosion law. Further studies will focus on these influencing factors with the modification of the erosion law.

5 Conclusions

A CFD-DEM coupling approach was used to model the suffusion process of gap-graded soils and mechanical tests to investigate the effect of the direction angles between seepage and gravity. Several numerical tests were carried out with different values of α_g that varied from 0° to 180°. In addition, two representative FCs (15% and 35%) were considered for all the cases. The key concluding remarks are as follows:

1. During the suffusion, the fines detachment, transportation and clogging mechanisms are significantly affected by the gravity and α_g. More attention should be paid to this fact in practical engineering considering that suffusion might occur in any direction.
2. By comparing the results from both macroscopic and microscopic scales, different force-chain transmission modes of FC = 15% and 35% are verified. The major force chain is transferred by coarse particles in the FC = 15% samples, while in the FC = 35% samples, the major force chain is mainly carried by fine particles.
3. Consequently, the effects of the angle between the flow and gravity directions were investigated from both macroscopic and microscopic points of view. The effect of erosion on granular soils requires attention to be paid to not only the initiation of erosion but also the development of erosion and the consequent mechanical behavior of soils.
4. Taking advantage of the CFDEM method, which can capture both micro- and macro-characteristics of particle and fluid, provides new insights into the microstructural origins underpinning the macroscopic mechanisms of suffusion.

Finally, this study provides both microscopic and macroscopic evidence for the proposal of further phenomenological or micromechanical models in order to solve multiphysics and multiscale engineering problems.

Acknowledgements The financial supports provided by the GRF project (Grant No. 15209119) and FDS project (Grant No. UGC/FDS13/E06/18) from Research Grants Council (RGC) of Hong Kong are gratefully acknowledged.

References

1. Benamar A, dos Santos RNC, Bennabi A, Karoui T (2019) Suffusion evaluation of coarse-graded soils from Rhine dikes. Acta Geotechnica 14(3):815–823
2. Bonelli S, Marot D (2008) On the modelling of internal soil erosion. In: The 12th international conference of international association for computer methods and advances in geomechanics (IACMAG), pp 7–14
3. Chand R, Khaskheli MA, Qadir A, Ge B, Shi Q (2012) Discrete particle simulation of radial segregation in horizontally rotating drum: Effects of drum-length and non-rotating end-plates. Phys A Stat Mech Appl 391(20):4590–4596
4. Chang DS, Zhang LM (2011) A stress-controlled erosion apparatus for studying internal erosion in soils. Geotech Test J 34(6):579–589
5. Chang DS, Zhang LM (2012) Critical hydraulic gradients of internal erosion under complex stress states. J Geotech Geoenviron Eng 139(9):1454–1467
6. Chareyre B, Cortis A, Catalano E, Barthélemy E (2012) Pore-scale modeling of viscous flow and induced forces in dense sphere packings. Transp Porous Media 94(2):595–615
7. Chen F, Drumm EC, Guiochon G (2011) Coupled discrete element and finite volume solution of two classical soil mechanics problems. Comput Geotech 38(5):638–647
8. Cook BK, Noble DR, Williams JR (2004) A direct simulation method for particle-fluid systems. Eng Comput 21(4):151–168
9. Cui X, Li J, Chan A, Chapman D (2014) Coupled DEM-LBM simulation of internal fluidisation induced by a leaking pipe. Powder Technol 254:299–306

10. Cundall PA, Strack OD (1979) A discrete numerical model for granular assemblies. Geotechnique 29(1):47–65
11. El Shamy U, Zeghal M, Dobry R, Thevanayagam S, Elgamal A, Abdoun T, Medina C, Bethapudi R, Bennett V (2010) Micromechanical aspects of liquefaction-induced lateral spreading. Int J Geomech 10(5):190–201
12. Ergun S (1952) Fluid flow through packed columns. Chem Eng Prog 48:89–94
13. Fannin R, Moffat R (2006) Observations on internal stability of cohesionless soils. Geotechnique 56(7):497–500
14. Fell R, Fry JJ (2014) The state of the art of assessing the likelihood of internal erosion of embankment dams, water retaining structures and their foundations. In: Internal erosion of dams and their foundations, CRC Press, pp 9–32
15. Feng Y, Han K, Owen D (2007) Coupled lattice Boltzmann method and discrete element modelling of particle transport in turbulent fluid flows: computational issues. Int J Numer Methods Eng 72(9):1111–1134
16. Goniva C, Kloss C, Hager A, Pirker S (2010) An open source CFD-DEM perspective. In: Proceedings of OpenFOAM workshop, Göteborg, pp 1–10
17. Guo Y, Yu XB (2017) Comparison of the implementation of three common types of coupled CFD-DEM model for simulating soil surface erosion. Int J Multiphase Flow 91:89–100
18. Hicher PY (2013) Modelling the impact of particle removal on granular material behaviour. Géotechnique 63(2):118–128
19. Hosn RA, Sibille L, Benahmed N, Chareyre B (2018) A discrete numerical model involving partial fluid-solid coupling to describe suffusion effects in soils. Comput Geotech 95:30–39
20. Hu Z, Zhang Y, Yang Z (2019) Suffusion-induced deformation and microstructural change of granular soils: a coupled CFD-DEM study. Acta Geotechnica 14(3):795–814
21. Issa RI (1986) Solution of the implicitly discretised fluid flow equations by operator-splitting. J Comput Phys 62(1):40–65
22. Issa RI, Gosman A, Watkins A (1986) The computation of compressible and incompressible recirculating flows by a non-iterative implicit scheme. J Comput Phys 62(1):66–82
23. Kawano K, Shire T, O'Sullivan C (2018) Coupled particle-fluid simulations of the initiation of suffusion. Soils Foundations 58(4):972–985
24. Ke L, Takahashi A (2012) Strength reduction of cohesionless soil due to internal erosion induced by one-dimensional upward seepage flow. Soils Foundations 52(4):698–711
25. Ke L, Takahashi A (2014) Experimental investigations on suffusion characteristics and its mechanical consequences on saturated cohesionless soil. Soils Foundations 54(4):713–730
26. Kloss C, Goniva C, Hager A, Amberger S, Pirker S (2012) Models, algorithms and validation for opensource DEM and CFD-DEM. Prog Comput Fluid Dyn Int J 12(2–3):140–152
27. Koch DL, Hill RJ (2001) Inertial effects in suspension and porous-media flows. Ann Rev Fluid Mech 33(1):619–647
28. Koch DL, Sangani AS (1999) Particle pressure and marginal stability limits for a homogeneous monodisperse gas-fluidized bed: kinetic theory and numerical simulations. J Fluid Mech 400:229–263
29. Li X, Zhao J (2018) Dam-break of mixtures consisting of non-Newtonian liquids and granular particles. Powder Technol 338:493–505
30. Liu YJ, Li G, Yin ZY, Dano C, Hicher PY, Xia XH, Wang JH (2014) Influence of grading on the undrained behavior of granular materials. Comptes Rendus Mécanique 342(2):85–95
31. Luo Y, Huang Y (2020) Effect of open-framework gravel on suffusion in sandy gravel alluvium. Acta Geotechnica 1–16 (In press)
32. Luo Y, Luo B, Xiao M (2019) Effect of deviator stress on the initiation of suffusion. Acta Geotechnica 15:1607–1617
33. Marot D, Rochim A, Nguyen HH, Bendahmane F, Sibille L (2016) Assessing the susceptibility of gap-graded soils to internal erosion: proposition of a new experimental methodology. Natural Hazards 83(1):365–388
34. Moffat R, Fannin RJ, Garner SJ (2011) Spatial and temporal progression of internal erosion in cohesionless soil. Canadian Geotech J 48(3):399–412
35. Muir Wood D, Maeda K (2008) Changing grading of soil: effect on critical states. Acta Geotechnica 3(1):3
36. Muir Wood D, Maeda K, Nukudani E (2010) Modelling mechanical consequences of erosion. Géotechnique 60(6):447–457
37. Nguyen CD, Benahmed N, Andò E, Sibille L, Philippe P (2019) Experimental investigation of microstructural changes in soils eroded by suffusion using X-ray tomography. Acta Geotechnica 14(3):749–765
38. Pianet G, Ten Cate A, Derksen J, Arquis E (2007) Assessment of the 1-fluid method for DNS of particulate flows: Sedimentation of a single sphere at moderate to high Reynolds numbers. Comput Fluids 36(2):359–375
39. Plimpton S (1995) Fast parallel algorithms for short-range molecular dynamics. J Comput Phys 117(1):1–19
40. Richards KS, Reddy KR (2007) Critical appraisal of piping phenomena in earth dams. Bull Eng Geology Environ 66(4):381–402
41. Scholtès L, Hicher PY, Sibille L (2010) Multiscale approaches to describe mechanical responses induced by particle removal in granular materials. Comptes Rendus Mécanique 338(10–11):627–638
42. Shan T, Zhao J (2014) A coupled CFD-DEM analysis of granular flow impacting on a water reservoir. Acta Mechanica 225(8):2449–2470
43. Sherard JL, Dunnigan LP, Talbot JR (1984) Basic properties of sand and gravel filters. J Geotech Eng 110(6):684–700
44. Skempton A, Brogan J (1994) Experiments on piping in sandy gravels. Geotechnique 44(3):449–460
45. Slangen P, Fannin R (2016) A flexible wall permeameter for investigating suffusion and suffosion. Geotechnical Test J 40(1):1–14
46. Šmilauer V, Catalano E, Chareyre B, Dorofenko S, Duriez J, Gladky A, Kozicki J, Modenese C, Scholtès L, Sibille L, Stránsky J, Thoeni K (2010) Yade reference documentation. In: Smilauer V (ed) Yade documentation, 1st edn. The Yade Project. http://yade-dem.org/doc/
47. Sterpi D (2003) Effects of the erosion and transport of fine particles due to seepage flow. Int J Geomech 3(1):111–122
48. Taha H, Nguyen NS, Marot D, Hijazi A, Abou-Saleh K (2019) Micro-scale investigation of the role of finer grains in the behavior of bidisperse granular materials. Granular Matter 21(2):28
49. Tao H, Tao J (2017) Quantitative analysis of piping erosion micro-mechanisms with coupled cfd and dem method. Acta Geotechnica 12(3):573–592
50. Terzaghi K (1922) The failure of dams by piping and its prevention. Die Wasserkr 17:445–449
51. Terzaghi K (1951) Theoretical soil mechanics. Chapman And Hall, Limited, London
52. Uzuoka R, Ichiyama T, Mori T, Kazama M (2012) Hydro-mechanical analysis of internal erosion with mass exchange between solid and water. In: Proceedings of 6th international conference on scour and erosion, pp 655–662
53. Van Buijtenen MS, Van Dijk WJ, Deen NG, Kuipers J, Leadbeater T, Parker D (2011) Numerical and experimental study on multiple-spout fluidized beds. Chem Eng Sci 66(11):2368–2376

54. Vardoulakis I, Stavropoulou M, Papanastasiou P (1996) Hydromechanical aspects of the sand production problem. Transp Porous Media 22(2):225–244
55. Wang M, Feng Y, Pande G, Chan A, Zuo W (2017) Numerical modelling of fluid-induced soil erosion in granular filters using a coupled bonded particle lattice boltzmann method. Comput Geotech 82:134–143
56. Wautier A, Bonelli S, Nicot F (2018) Flow impact on granular force chains and induced instability. Phys Rev E 98(4):042909
57. Xiong H, Nicot F, Yin Z (2017) A three-dimensional micromechanically based model. Int J Numer Anal Methods Geomech 41(17):1669–1686
58. Xiong H, Nicot F, Yin Z (2019) From micro scale to boundary value problem: using a micromechanically based model. Acta Geotechnica 14(5):1307–1323
59. Xiong H, Yin ZY, Nicot F (2019) A multiscale work-analysis approach for geotechnical structures. Int J Numer Anal Methods Geomech 43(6):1230–1250
60. Yang J, Yin ZY, Laouafa F, Hicher PY (2019) Internal erosion in dike-on-foundation modeled by a coupled hydromechanical approach. Int J Numer Anal Methods Geomech 43(3):663–683
61. Yin ZY, Chang CS, Hicher PY (2010) Micromechanical modelling for effect of inherent anisotropy on cyclic behaviour of sand. Int J Solids Struct 47(14–15):1933–1951
62. Yin ZY, Zhao J, Hicher PY (2014) A micromechanics-based model for sand-silt mixtures. Int J Solids Struct 51(6):1350–1363
63. Yin ZY, Huang HW, Hicher PY (2016) Elastoplastic modeling of sand-silt mixtures. Soils Foundations 56(3):520–532
64. Zhang DM, Gao CP, Yin ZY (2019) CFD-DEM modeling of seepage erosion around shield tunnels. Tunnell Underground Space Technol 83:60–72
65. Zhao J, Guo N (2013) Unique critical state characteristics in granular media considering fabric anisotropy. Géotechnique 63(8):695–704
66. Zhao J, Shan T (2013) Coupled CFD-DEM simulation of fluid-particle interaction in geomechanics. Powder Technol 239:248–258
67. Zhong C, Le VT, Bendahmane F, Marot D, Yin ZY (2018) Investigation of spatial scale effects on suffusion susceptibility. J Geotech Geoenviron Eng 144(9):04018067
68. Zhou C, Ooi JY (2009) Numerical investigation of progressive development of granular pile with spherical and non-spherical particles. Mech Mater 41(6):707–714
69. Zhou Y, Wright B, Yang R, Xu BH, Yu AB (1999) Rolling friction in the dynamic simulation of sandpile formation. Phys A Stat Mech Appl 269(2–4):536–553
70. Zhou Z, Kuang S, Chu K, Yu A (2010) Discrete particle simulation of particle-fluid flow: model formulations and their applicability. J Fluid Mech 661:482–510
71. Zhou Z, Yu A, Choi S (2011) Numerical simulation of the liquid-induced erosion in a weakly bonded sand assembly. Powder Technol 211(2–3):237–249